Supporting Information

Absolute photoluminescence quantum yields of IR-emissive $Cd_{1-x}Hg_xTe$ and PbS quantum dots – Method- and material-inherent challenges

*Soheil Hatami[a], Christian Würth[a], Martin Kaiser[a], Susanne Leubner[b], Stefanie Gabriel[b], Lydia Bahrig[b], Vladimir Lesnyak[b,c], Jutta Pauli[a], Nikolai Gaponik[b], Alexander Eychmüller[b], Ute Resch-Genger[a]**

[a] BAM Federal Institute for Materials Research and Testing, Richard-Willstaetter-Str. 11, 12489 Berlin, Germany

[b] Physical Chemistry and Center for Advancing Electronics Dresden, TU Dresden, Bergstr. 66b, 01062 Dresden, Germany

[c] Department of Nanochemistry, Istituto Italiano di Tecnologia, via Morego, 30, 16163 Genova, Italy

* Email: ute.resch@bam.de

Organic NIR fluorophores

The chemical structures of the NIR dye IR140 and IR26 are shown in Figure 1S.

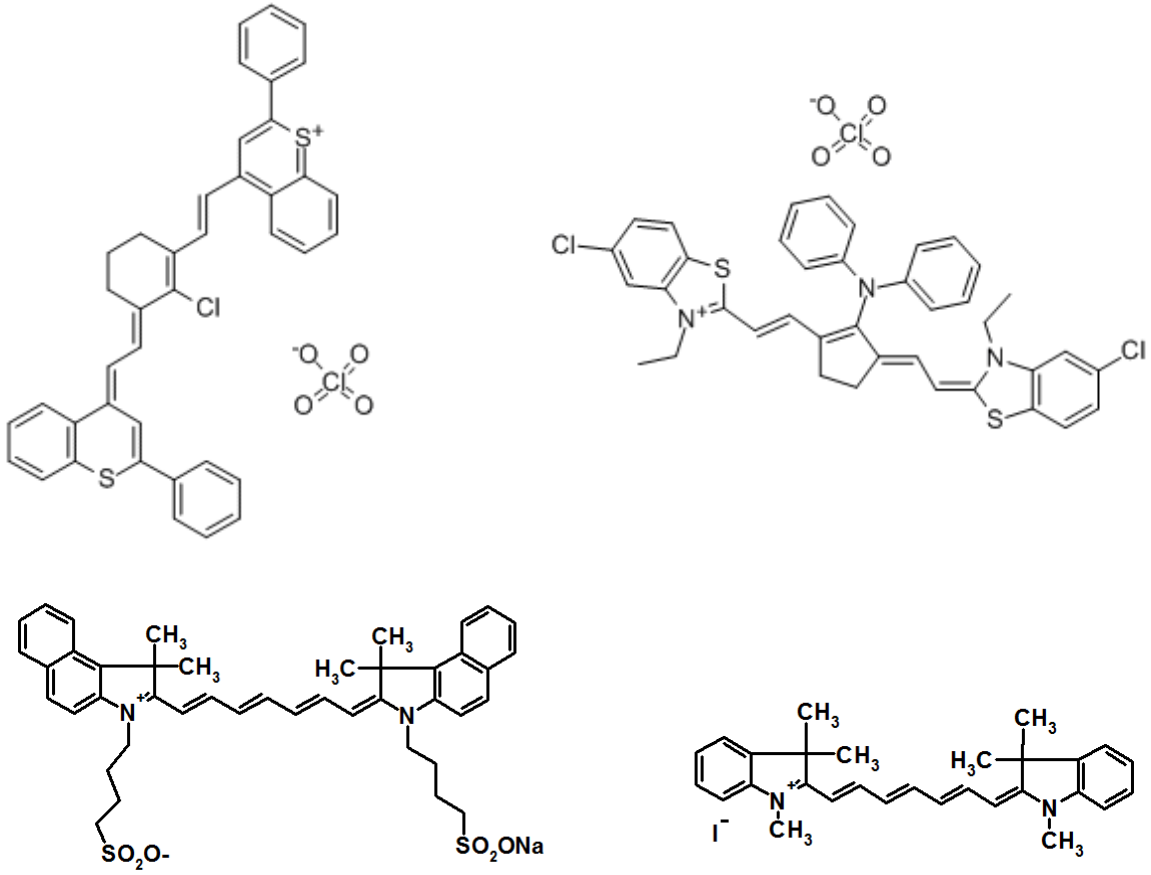

Figure 1S. Chemical structures of the dyes IR26 (left, top) and IR140 (right, top), both used as perchlorates as well as IR125 (left bottom) and HITCI (right bottom.

Physical standards for instrument calibration

The wavelength accuracy of the integrating sphere setups and spectrofluorometer FSP 920 was determined with a low pressure mercury/argon discharge lamp CAL-2000 (Ocean Optics Inc.).[1] A calibrated quartz halogen lamp mounted inside a sphere (Gigahertz-Optik GmbH; PTB-calibrated wavelength dependence of the spectral radiance ($L_\lambda(\lambda)$; termed SDS) was used for the determination of the spectral responsivities ($s(\lambda_{em})$) of the UV/vis/NIR and NIR/IR integrating spheres as well as a black body radiator (CI

Systems SR-2; temperature control of spectral radiance; termed BBR; operated at T = 1200 °C) for the latter. The very smooth emission spectrum of the BBR was calculated according to Planck´s law for this known blackbody temperature. Neutral density filters of known transmission from Starna Ltd. and calibrated neutral density filters from Hellma GmbH were employed for the determination of the linear range of the CCD detectors of the integrating sphere setups and the calibration of the photometer, respectively.

Relative fluorescence measurements

For spectrally resolved relative measurements of fluorescence intensities in the wavelength region of 300 – 1700 nm, a calibrated Edinburgh Instruments FSP 920 spectrofluorometer equipped with double monochromators (with different wavelength-adapted gratings) and three detectors (photomultiplier tube (PMT) R928 from Hamamatsu for the wavelength region of 300 – 850 nm, PMT R2658P from Hamamatsu for the wavelength region of 300 – 1100 nm, and nitrogen-cooled PMT R5509P from Hamamatsu for the wavelength region of 700 – 1750 nm, respectively) with polarizers in the excitation and emission channel(s) set to 0° and 54.7° was used. The exciting radiant power of the xenon lamp monochromator ensemble used for relative measurements of photoluminescence was commonly 0.1 mW in the wavelength region of 630 nm to 785 nm for typically used slit widths of the monochromator.

Calibration of spectrofluorometer FSP 920. This included the determination of the wavelength accuracy, the linearity of the detection system and the determination of the spectral responsivity $s(\lambda_{em})$ (spectral emission correction) was performed with calibration

accessories from the instrument manufacturer Edinburgh Instruments, i.e., a calibrated white standard and a calibrated spectral radiance transfer standard and procedures previously described for our spectrofluorometer 8100 SLM.[1-3] Three alterations were introduced in the determination of $s(\lambda_{em})$. To avoid distortion of the emission characteristics of the calibrated lamp by absorption of water vapor in the air, the lamp was closely attached to the nitrogen-purged sample compartment. To prevent detector saturation, the spectral radiant power of the lamp reaching the detection channel was reduced with a metal-mesh optical filter. Order diffractions were eliminated via a longpass (LP) filter. Prior to the determination of the spectral correction curves, the wavelength accuracy of the spectrometer was controlled and the linearity of each detector was determined following a previously reported procedure.[2]

Relative measurement of Φ_f. Relatively measured Φ_f values using the previously evaluated dyes HITCI (solvent ethanol (EtOH); $\Phi_f = 0.30$)[4] and IR125 (solvent dimethylsulfoxide (DMSO); $\Phi_f = 0.23$)[4] as reference were calculated according to the formula of Demas and Crosby,[5] see equation 1S, from fluorescence emission spectra, blank-corrected and corrected for instrument-specific effects relative to the spectral radiance scale.[1, 2, 6] For IR26, the emission spectra were corrected for dye reabsorption and solvent absorption as detailed in the section on corrections performed for absolute measurements of Φ_f (see also Figure 8S). The emission spectra were then multiplied by hc/λ_{em} to render them traceable to the spectral photon radiance photonic units.[1, 2] Hence, Φ_f can be directly obtained from the integration of these emission spectra.[7] The subscripts x and st denote sample and standard and the subscript ex excitation. $\Phi_{f,st}$ equals the fluorescence quantum yield of the standard, typically taken from the literature.

$$\Phi_{f,x} = \Phi_{f,st} \cdot \frac{F_x}{F_{st}} \cdot \frac{f_{st}(\lambda_{ex,st})}{f_x(\lambda_{ex,x})} \cdot \frac{n_x^2(\lambda_{ex,x})}{n_{st}^2(\lambda_{ex,st})} \qquad \text{(eq. 1S)}$$

The absorption factor $f(\lambda_{ex})$ in equation 1S provides the fraction of the excitation light absorbed by the chromophore (see equation 2S).[8] $f(\lambda_{ex})$ is linked to absorbance $A(\lambda_{ex})$ and thus, to the molar decadic absorption coefficient ε of the chromophore (at the excitation wavelength λ_{ex}), its concentration c and to the path length l.

$$f(\lambda_{ex}) = 1 - T(\lambda_{ex}) = 1 - 10^{-A(\lambda_{ex})} = 1 - 10^{-\varepsilon(\lambda_{ex})cl} \qquad \text{(eq. 2S)}$$

F equals the integrated spectral fluorescence photon flux $q_{p,\lambda}^{f}(\lambda_{em})$ at the detector, see equation 3S, obtained from blank and dark-count corrected signals of the emission detector $I_u(\lambda_{em})$ multiplied with the photon energy hc_0/λ_{em} (h: Planck constant, c_0: velocity of light in vacuo) and divided by the instrument´s spectral responsivity $s(\lambda_{em})$.[1] For the refractive index n, wavelength-dependent refractive indices were employed.

$$F = \int_{\lambda_{em1}}^{\lambda_{em2}} q_{p,\lambda}^{f}(\lambda_{em})\, d\lambda_{em} = (hc_0)^{-1} \int_{\lambda_{em1}}^{\lambda_{em2}} \frac{I_u(\lambda_{em})}{s(\lambda_{em})} \lambda_{em}\, d\lambda_{em} \qquad \text{(eq. 3S)}$$

The absorption and normalized emission spectra of the dyes HITCI in ethanol and IR125 in DMSO used as references for relative measurements of $Cd_xHg_{1-x}Te$ and an exemplarily chosen PbS colloid are shown in Figure 2S providing the commonly used excitation wavelengths. For relative measurements of Φ_f with different excitation wavelengths for sample and standard as performed e.g., in the case of IR26 determined relatively to IR125, we used an excitation correction curve determined with a calibrated

detector at sample position as previously described, thereby considering the different excitation photon fluxes.[9] The Φ_f were then calculated as described by Würth et al..[9]

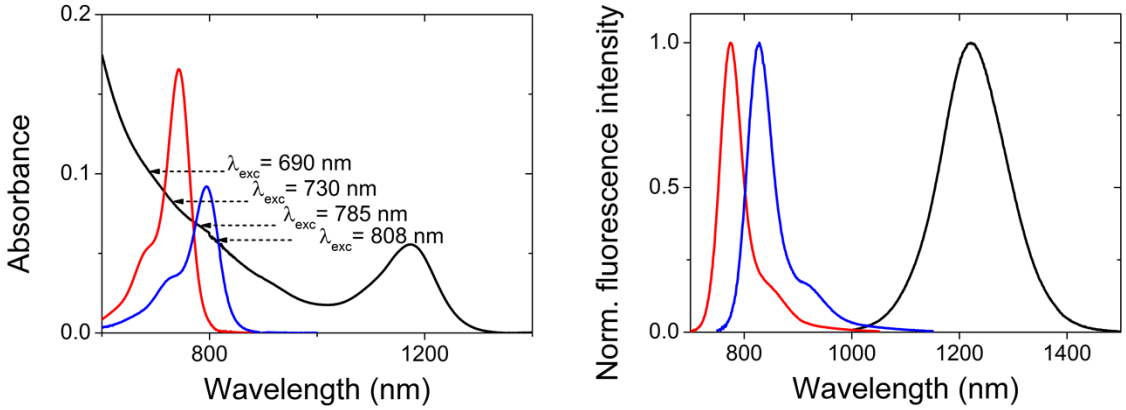

Figure 2S Absorption and normalized corrected emission spectra of a PbS colloid (black line) and the dyes HITCI (solvent EtOH; red line) and IR125 (solvent DMSO; blue line) used as references for relative measurements of Φ_f. The excitation wavelengths are given in the left panel.

Absolute measurement of Φ_f

We employed a previously described calibrated UV/vis/NIR integrating sphere setup equipped with a silicon charge coupled device (CCD) for absolute measurements of photoluminescence and Φ_f in the wavelength region of 350 – 1050 nm[10] and our new NIR/IR integrating sphere setup detailed in the ms.

NIR/IR integrating sphere setup. Here, only more details on commercial setup components of this setup up shown (Figure 1) and described in the ms are given.We used a f/4 Czerny Turner imaging spectrograph (Shamrock 303i, Andor Technology PLC;

diffraction grating blazed at 1250 nm, 150 lines/mm) attached to a Peltier cooled (188 K), thinned back side illuminated deep depletion InGaAs charge coupled device (iDus InGaAs 1.7 µm DU491A, Andor Technology PLC; CCD line, 1024×1 pixel, pixel sizes of 25 µm×500 µm) with quantum efficiencies of > 85 % in the spectral range of 1100 – 1500 nm and > 20 % at shorter wavelengths and longer wavelengths (up to 1700 nm) as detection system.

Measurement procedure. The absolute determination of Φ_f with an integrating sphere setup includes the following steps: i.) measurement of the transmitted incident radiant power and the emission spectrum of the sample (here fluorophore in a solvent) and a blank (solvent-filled cuvette) under identical measurement conditions (e.g., excitation wavelength, temperature, cell position), each within a single scan, ii.) data evaluation including choice of the excitation and emission wavelength region for spectral emission correction and signal integration, and iii.) calculation of Φ_f using equation 4S.[9, 10] Here, λ_{ex} and λ_{em} are the excitation and emission wavelength, respectively, I presents the measured, dark count-corrected and spectrally uncorrected spectrum and $s(\lambda_{ex})$ and $s(\lambda_{em})$ the spectral responsivities of the detection channel within the wavelength region of excitation, respectively. The difference between the transmitted radiant power of the blank ($I_b(\lambda_{ex})$) and the sample ($I_s(\lambda_{ex})$) within the spectral region of the excitation bandpass $\Delta\lambda_{ex}$ yields the number of absorbed photons. Integration of the blank-corrected and spectrally corrected emission spectrum of the sample ($I_s(\lambda_{em})$ - $I_b(\lambda_{em})$) provides the number of emitted photons.

$$\Phi_f = \frac{\int_{\lambda_{em1}}^{\lambda_{em2}} \left(\frac{I_s(\lambda_{em}) - I_b(\lambda_{em})}{s(\lambda_{em})} \right) \lambda_{em} d\lambda_{em}}{\int_{\lambda_{ex}-\Delta\lambda}^{\lambda_{ex}+\Delta\lambda} \left(\frac{I_b(\lambda_{ex}) - I_s(\lambda_{ex})}{s(\lambda_{ex})} \right) \lambda_{ex}\, d\lambda_{ex}} = \frac{N_{em}}{N_{abs}} \qquad \text{(eq. 4S)}$$

Data analysis of integrating sphere measurements. Data processing includes the combination of the data recorded with different positions of the gratings of the emission monochromator to a single spectrum (termed also spectral "glueing"), data interpolation (equally spaced data points of 0.5 nm), and for dye and NC samples, blank and spectral correction of the measured data.[1, 2] This was realized with the Andor Solis Imaging and Spectrograph Software.

Calibration of the integrating sphere setups with physical transfer standards (PTS)

The calibration of the UV/vis/NIR integrating sphere setup was performed as recently reported[10] using the previously described calibration equipment. The calibration of the NIR/IR integration sphere setup is subsequently described.

Wavelength accuracy. For the control of the wavelength accuracy of the emission monochromator of the NIR/IR integrating sphere setup with the low pressure mercury/argon discharge lamp (using first, second and third orders diffractions of the emission lines), the grating offsets of the spectrograph were adjusted until the spectral positions of the detected emission lines matched the values reported for this wavelength standard (NIST Physical Reference Data: http://physics.nist.gov/PhysRefData/Handbook/Tables/mercurytable2.htm and

http://physics.nist.gov/PhysRefData/Handbook/Tables/argontable2.htm). The results shown in Figure 3S underline the wavelength accuracy of the detection channel of our integrating sphere setup. The spectral resolution of the detection channel of our NIR/IR integrating sphere setup in this configuration is *ca*. 1 nm.

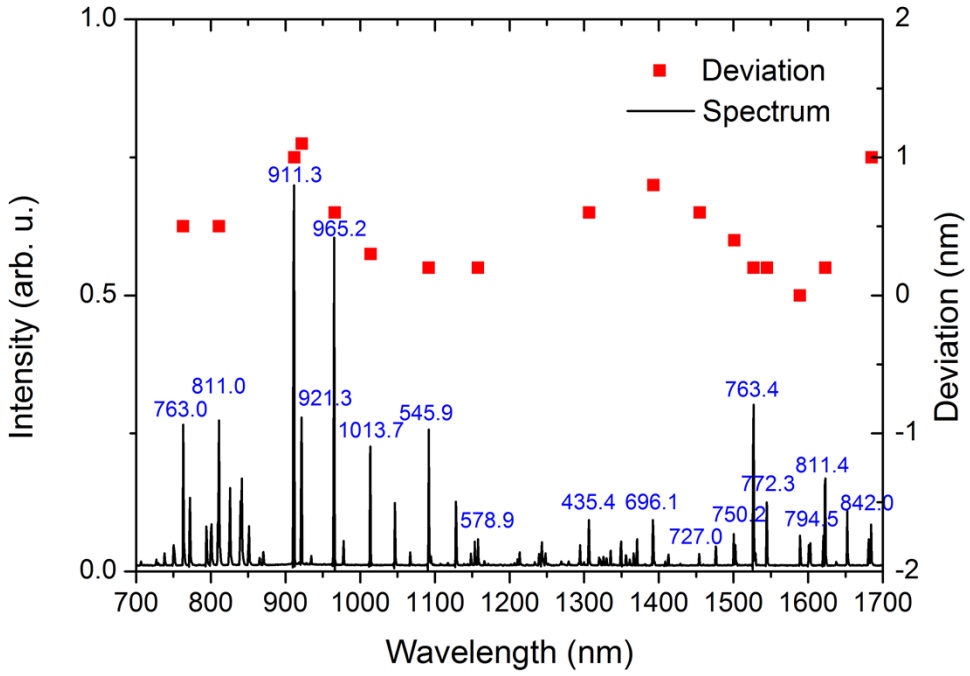

Figure 3S Wavelength accuracy of the NIR/IR integrating sphere setup in the wavelength region of 700 – 1700 nm. The spectral deviations from the peak positions taken from the NIST Physical Reference Data are given as squares. The peak positions (blue numbers) are in given in nm.

Linear range of detection. This parameter is of special importance, as the transmitted spectral radiant power of the excitation light and the emitted spectral radiant power

measured during the course of the absolute determination of Φ_f with an integrating sphere can differ by a factor of more than hundred. The linear range of the InGaAs-CCD detector was obtained by controlled variation of the radiant power of the different laser diodes used with a set of calibrated neutral density filters (known transmission) in a filter wheel placed in front of the integrating sphere as excitation light sources and hence, of the radiant power reaching the detector. This is shown in Figure 4S, which illustrates the excellent linearity of the detection system of the integrating sphere setup amounting to 0.3 % in the spectral range of 690 nm to 915 nm for the whole dynamic range of about 60,000 counts/s (set to one).

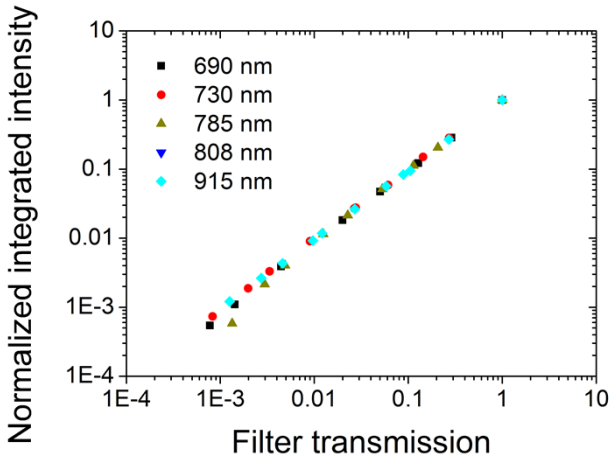

Figure 4S. Linearity of the detection channel of the NIR/IR integrating sphere setup measured at different wavelength using various laser diodes attenuated with different calibrated neutral density filters. Signal integration was always carried out over the same pixel columns located in the middle of the InGaAs-CCD array. The count rate of 60,000 counts/s was set to one.

Longterm stability of the excitation light sources. For the determination of the longterm stability of the different excitation light sources, for each laser diode, the

radiance of the sphere wall was recorded multiple times under the same measurement conditions (integration time, number of accumulations) as used for typical Φ_f measurements. The resulting relative deviations of the mean values (integration over the entire peak) are shown in Figure 5S exemplarily for four laser diodes, underlining the generally small size of these intensity fluctuations below 1 %. This is very important for small measurement uncertainties.

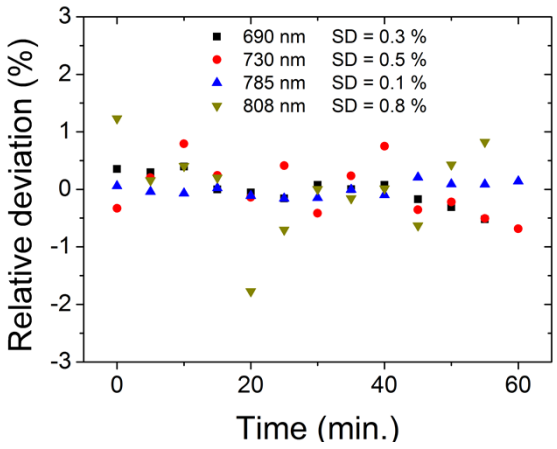

Figure 5S Longterm stability of exemplarily chosen laser diodes given as standard deviations (SD) obtained from time-dependent measurements of the radiance of the sphere wall under the same measurement conditions (1000 accumulations (acc.), 0.02 sec integration time) as used for typical Φ_f measurements.

Spectral responsivity. $s(\lambda_{em})$ of the new integrating sphere setup was determined with two calibrated light sources, a quartz halogen lamp placed inside an integrating sphere (SDS; emission maximum at 1050 nm)) as previously described. As an alternative calibration strategy and to control the reliability of the emission correction curves

obtained with the SDS, we determined $s(\lambda_{em})$ also with a blackbody radiator (BBR), that presents an interesting alternative to a SDS especially at longer wavelengths in the NIR/IR where the spectral radiance of the SDS is decreasing. For the conditions used here (1200 °C), the BBR has an emission maximum at 1970 nm.

Critical for the accurate determination of $s(\lambda_{em})$ with these calibration lamps over such a the very broad spectral region of 600 – 1600 nm was the elimination of second order diffractions and stray light, especially for the single monochromator used here. This was achieved with different long pass (LP) interference filters (cut-on wavelengths of 600, 800, 950, and 1000 nm) chosen individually for each excitation light source and calibration lamp and spectral region to be covered.

For the determination of $s(\lambda_{em})$, relying on a known linearity of the detection system, defined grating positions for each part of the spectrum were used. The single spectra obtained for the two calibration lamps and the different (LP) filters within different comparatively narrow wavelength regions were subsequently merged with the described "glueing" procedure to a continuous spectrum $S_{em}(\lambda)$. Division of the signal of the emission detector $S_{em}(\lambda)$ by the (relative) spectral radiance of the calibrated lamp yields the (relative) spectral responsivity $s(\lambda_{em})$, see equation 6S. Division of the measured raw emission spectra (blank corrected, i.e., corrected for background signals) by $s(\lambda_{em})$ subsequently leads to corrected emission spectra $I_c(\lambda_{em})$.

$$s(\lambda_{em}) = \frac{S_{em}(\lambda_{em})}{L_{\lambda}(\lambda_{em})} \qquad \text{(eq. 6S)}$$

For control of the complete removal of water vapor (absorption spectrum shown in Figure 7S) during instrument calibration and check on possible contributions from water

vapor absorption in the wavelength region relevant for calibration, the emission correction curves (equaling here $1/s(\lambda_{em})$) were always controlled for the appearance of absorption bands / spectral features at *ca*. 930 – 980 nm, 1120 – 1160 nm, and *ca*. 1350 – 1500 nm characteristic for water.

An example for the determination of emission correction curves is shown in Figure 6S, displaying the resulting emission correction curves generated from measurements with the SDS and the BBR with a 800 nm LP filter. As the emission maxima of the SDS and the BBR are located at 1050 nm and 1970 nm, respectively, at 800 nm, stray light arises mainly from the BBR and at 1600 nm, contributions from the second order diffractions of the SDS emission can be noticed. For the eventually generated combined emission correction curve, we used the emission correction curve measured with the SDS in the wavelength region of 600 – 950 nm and the emission correction curve measured with the BBR in the wavelength region of 950 – 1600 nm. This was done analogously for the 600 nm, 950 nm, and 1000 nm LP filters, thereby generating correction curves for typically used measurement conditions.

Moreover, the comparison of the results obtained with the two calibration lamps provides automatically a tool to control the reliability of this critical calibration step. The good comparability of both instrument calibrations shown in Figure 6S underlines the reliability of our emission correction curves.

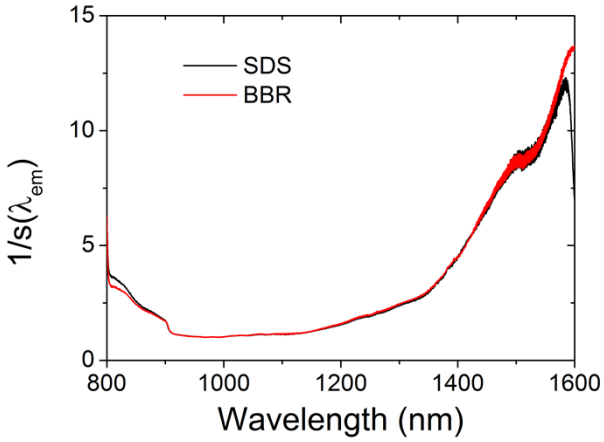

Figure 6S. Exemplified inverse spectral responsivity (equaling the emission correction curve) of the integrating sphere-detection system ensemble for a grating blazed at 1250 nm determined with two calibrated light sources, a quartz halogen lamp placed inside an integrating sphere (SDS; calibrated wavelength dependence of the spectral radiance Lλ(λ); black line) and a blackbody radiator (BBR; red line) operated at precisely known and measured temperatures, here T = 1200 °C. A 800 nm LP filter was used to eliminate second order diffractions for the exemplarily shown correction curves. For this exemplified combined emission correction curve, we used the emission correction curve measured with the SDS in the wavelength region of 600 nm to 950 nm and the emission correction curve measured with the BBR in the wavelength region of 950 nm to 1600 nm.

Water vapor absorption. To underline special problems in the IR region above 950 nm related to the presence of absorbing water vapor, the absorption of water vapor in the NIR and IR was simulated for given atmospheric conditions, i.e., summer and winter for high

latitude using the *Information System Spectroscopy of Atmospheric Gases* (http://spectra.iao.ru) (Figure 7S). The humidity and its fluctuations for this condition should be comparable with the conditions in our lab. Figure 7S reveals considerable differences in the absorption coefficient of water vapor between summer and winter. The temperature fluctuation does not considerably affect the water absorption coefficient. This clearly underlines the need to remove traces of water especially for measurements with integrating sphere setups where the many diffuse reflections of the exciting and emitted photons in the sphere result in considerable optical path lengths.

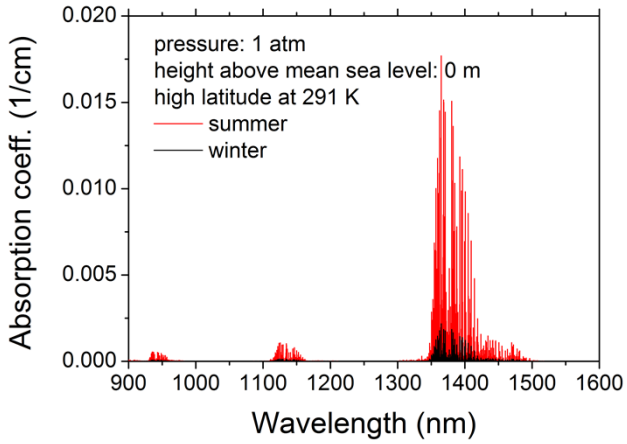

Figure 7S. Simulation of the absorption spectra / wavelength-dependent (molar decadic) absorption coefficients of water vapor in the NIR and IR exemplarily for in summer and winter for high latitude obtained with the help of the Information System Spectroscopy of Atmospheric Gases (http://spectra.iao.ru). The humidity and its fluctuations should be comparable with the conditions in our lab.

Aggregation studies with IR26 and concentration-dependent emission spectra

The very low Φ_f of IR26 required the use of higher dye concentrations (equaling absorbances of up to 0.8 at the absorption maximum of 1082 nm). To verify the absence of non-emissive dye aggregates at higher dye concentrations, we measured the concentration-dependent absorption spectra. From the matching normalized absorption spectra shown in Figure 8S (left panel), dimer formation can be excluded.

The red shift of the emission spectra of IR26 at higher dye concentrations shown in Figure 8S (right panel) is indicative of dye reabsorption. The dip at about 1170 nm originating from solvent absorption was corrected by consideration of the solvent absorption spectrum, yielding the solvent-corrected emission spectrum of this dye (dashed line) which was then used for the determination of Φ_f.

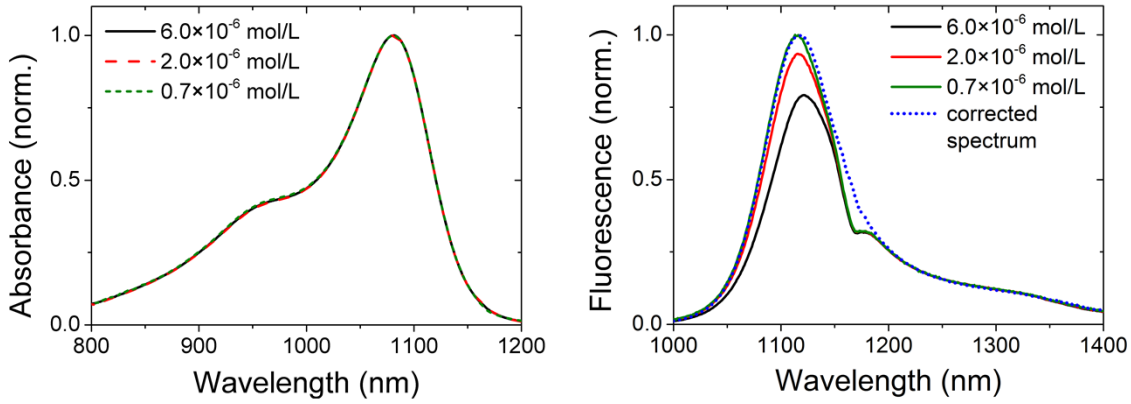

Figure 8S. Normalized absorption (left panel; normalized at maximum) and emission (right panel; normalized at 1250 nm) spectra of IR26 in DCE obtained for dye concentrations of 0.7×10^{-6} mol/L (absorbance A = 0.04 at the excitation wavelength (λ_{ex}) of 980 nm and A = 0.09 at the absorption maximum (λ_{max}) of 1082 nm), 2.0×10^{-6} mol/L ($A(\lambda_{ex}) = 0.13$, $A(\lambda_{max}) = 0.29$), and 6.0×10^{-6} mol/L ($A(\lambda_{ex}) = 0.36$, $A(\lambda_{max}) = 0.8$), respectively. In

the right panel, also the emission spectrum of IR26 measured for the lowest dye concentration and corrected for solvent absorption is included (dashed line).

Photostability studies

Photostability studies were performed with all organic dyes and the NIR/IR integrating sphere setup using the respective excitation light sources used for their measurement and typical radiant powers of 0.1 – 4 mW. In the case of the 980 nm laser diode, higher radiant powers of 690 and 1600 mW were used. Such measurements are exemplarily shown for IR140 and IR26 in Figure 9S. The diminution of the intensities of the absorbed and emitted light indicates photodecomposition and the slight increase in Φ_f is attributed to a decrease in dye reabsorption with decreasing dye concentration. Similar studies with semiconductor NC are shown for PbS in the ms and in one of the following sections in the *SI*.

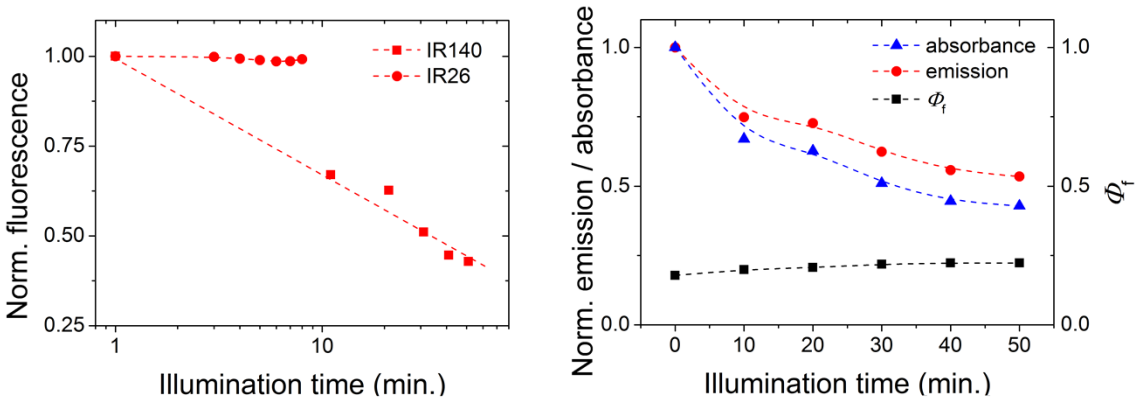

Figure 9S Left: Photostability (normalized fluorescence intensity) of IR140 in DMSO (red squares) and IR26 in DCE (red circles) measured with a 808 nm laser diode and a 980 nm laser diode using typical radiant powers of 4

mW (808 nm) and 1600 mW (980 nm), respectively. Right: Changes in the absorption intensity at the excitation wavelength (blue triangles), in the emission intensity (red circles), and the fluorescence quantum yield (black squares) upon illumination with a 808 nm laser diode exemplarily for IR140. The stability studies were performed with the NIR/IR integrating sphere setup enabling simultaneous measurements of changes in the absorbed and emitted photon fluxes. The dashed lines are shown only as a guide for the eye.

Corrections performed for absolute measurements of Φ_f

Fluorescence measurements with an integrating sphere setup are especially prone to reabsorption effects for samples with considerable overlap of absorption and emission and in the case of the NIR and IR region also to signal distorting solvent absorption. Such undesired signal contributions were taken into account as described in the following sections.

Consideration of sample reabsorption and solvent absorption. For samples with $\Phi_f < 0.1$, where the probability of reemission after reabsorption is small, and the use of a solvent absorbing at wavelength within the sample´s emission band as is the case for IR26 in DCE (see ms, Figure 3, right panel), we developed a new procedure that enables the consideration of both signal-distorting effects simultaneously. i.) First, we determined the undistorted corrected emission spectrum of a very diluted solution of IR26 in DCE (A = 0.004 at the absorption maximum, equaling a concentration of 3.3×10^{-8} M) the sample in a 0°/90° measurement geometry in a 10 mm×4 mm cell with spectrofluorometer FSP

920 using a 980 nm laser diode for excitation. The true spectrum of this dye solution was obtained by consideration of the absorption spectrum of the solvent measured with an absorption spectrometer, taking into account the different optical path length for fluorescence and absorption measurements. The spectral shape of this emission spectrum is assumed to reflect the true, not disturbed emission spectrum of the sample. ii.) Secondly, the spectrally corrected emission spectra of differently concentrated solutions of IR26, all distorted by reabsorption and solvent absorption (see Figure 8S, right panel) were obtained with the NIR/IR integrating sphere setup and the respective fraction of the absorbed light. iii.) The emission spectra determined with the integrating sphere were scaled in the wavelength region, where they are not distorted by solvent absorption and dye reabsorption, here from 1250 – 1300 nm (see ms, Figure 3, left panel) with the true emission spectrum. iv.) Subsequently, the number of emitted photons was obtained by integration of the rescaled spectrally corrected emission spectrum obtained with the NIR/IR integrating sphere.

Reabsorption correction for integrating sphere measurements. For moderately to highly fluorescent samples with $\Phi_f > 0.1$ and measurements in 10×10 mm cells, we employed a previously derived reabsorption-correction of the emission spectra of all NIR dyes except for Itrybe and all NC solutions (see equation 5S)[11, 12] for the calculation of absolute Φ_f values from measured blank and spectrally corrected emission spectra.

$$\Phi_{f,corr} = \frac{\Phi_{f,obs}}{1 - a + a\Phi_{f,obs}} \qquad \text{(eq. 5S)}$$

a in equation 5S characterizes the reabsorption probability. a was obtained by a comparison of undisturbed (spectrally corrected) emission spectra measured with our

spectrofluorometer and the disturbed (spectrally corrected) emission spectra determined with the integrating sphere spectrometer, using concentration series for each dye. Alternatively, smaller cells with an optical path length of 0.4 cm were used, thereby simultaneously reducing solvent absorption.

Size determination and spectroscopic properties of PbS colloids

The absorption spectra and corrected emission spectra of the differently sized PbS colloids directly measured after dilution of the respective PbS NC stock solutions with tetrachloroethylene (TCE) are shown in Figure 10S. The stock solutions were aged (stabilized) in air for *ca*. 300 days. These absorption spectra were used for the calculation of the size of the colloids as described by Cademartiri et al.,[13] yielding sizes of 2.3 nm, 4.1 nm, and 4.4 nm, respectively.

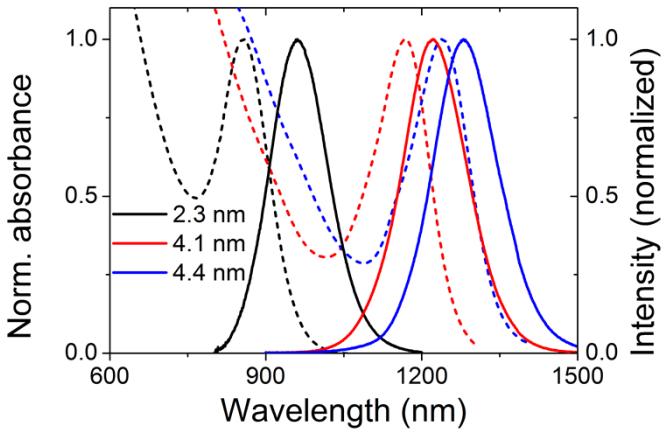

Figure 10S. Absorption (dashed lines) and normalized corrected emission (solid lines) spectra of 2.3 nm (black; concentration (c) of 3×10^{-6} mol/L), 4.1 nm (red; c = 6.3×10^{-7} mol/L), and 4.4 nm (blue; c = 6.1×10^{-7} mol/L) oleate-capped PbS colloids directly after dilution.

Thermal and photochemical stability studies with semiconductor NCs

The thermal and photochemical stability of all $Cd_xHg_{1-x}Te$ and PbS colloids was examined prior to absolute Φ_f measurements, using dilute solutions of these NCs freshly prepared from NC stock solutions and conventional spectrometers as well as the NIR/IR integrating sphere setup equipped with different intense laser diodes and lasers. Prior to these studies, an influence of dilution on the spectroscopic properties of these colloids was excluded.

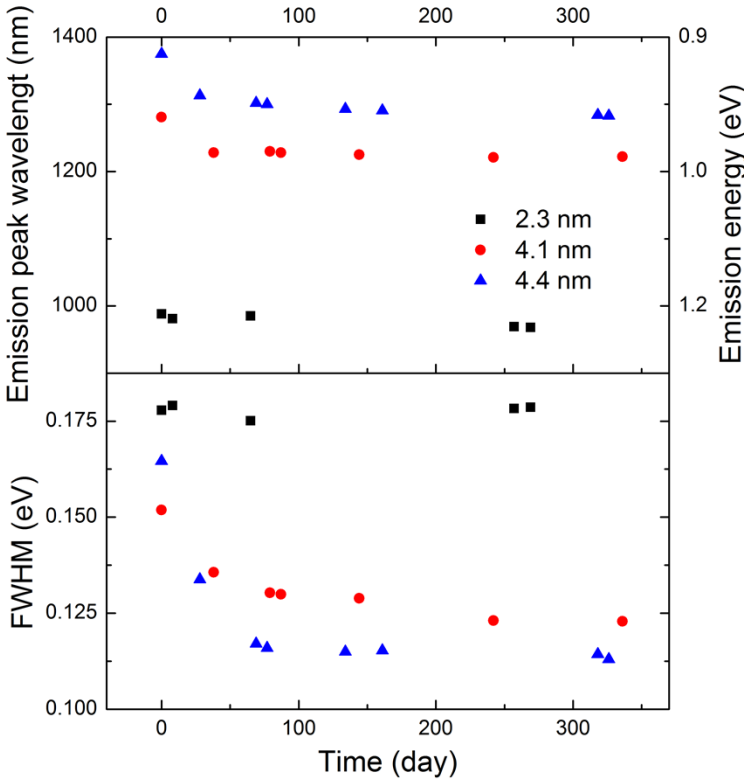

Figure 11S. Aging studies: Change in the spectral position of the emission band (upper panel) and in the emission band width (FWHM: full width at half height of

the maximum; lower panel) of 2.3 nm-, 4.1 nm-, and 4.3 nm-sized oleate-capped PbS stored in air at 4 °C in the dark as function of time.

Aging of PbS in air. Figure 11S summarizes the aging of 2.3 nm- and 4.1 nm-sized PbS colloids in air, showing the time-dependent changes in the emission maxima and the emission band widths, i.e., FWHM. 4.4. nm PbS revealed a change in FWHM from 0.165 eV to 0.113 eV (see are Figure 5 (top panel) in the ms) and 4.1 nm PbS from 0.152 eV to 0.123 eV, respectively. Contrary, for 2.3 nm PbS, both the spectral position of the emission maximum and FWHM (FWHM = 0.178 eV) barely changed after NC synthesis.

Photostability of PbS in air. Figure 12S illustrates the changes in absolutely measured Φ_f and in the spectral position of the emission band resulting for 2.3 nm-sized (left panel) and 4.1 nm-sized oleate-capped PbS (right panel), aged in air for *ca*. 300 days and diluted in TCE, as function of illumination time with the 808 nm laser diode of the integrating sphere setup (radiant power of 62 mW).

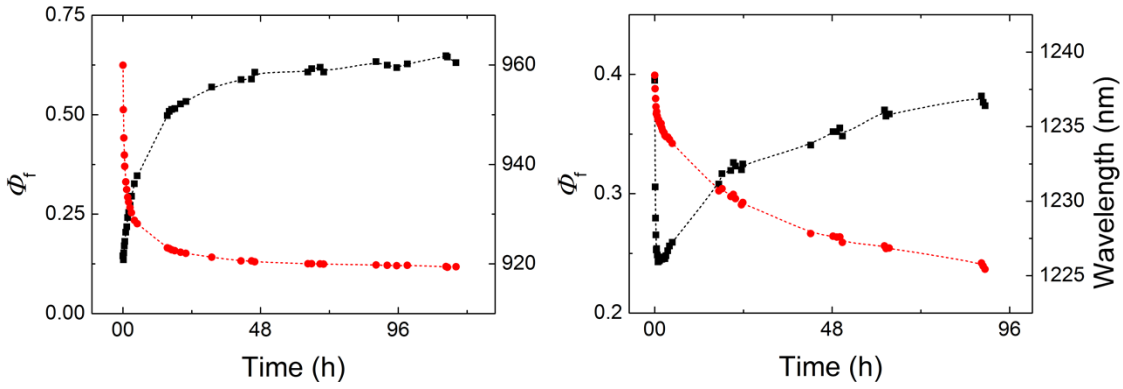

Figure 12S. Change in absolutely measured Φ_f (black symbols) and in the spectral position of the emission band (red symbols) of 2.3 nm-sized oleate-capped PbS (left panel) and 4.1 nm-sized oleate-capped PbS (right panel),

aged/stored in air in toluene for *ca*. 300 days and subsequently diluted in TCE as function of illumination time with the 808 nm laser diode of the integrating sphere setup (radiant power of 62 mW). The dashed lines are shown as a guide for the eye only.

The corresponding changes observed for 4.4 nm-sized PbS are given in the ms (see Figure 5).

References

1. U. Resch-Genger and P. C. DeRose, *Pure Applied Chemistry* 2012, 84, 1815-1835.
2. U. Resch-Genger, D. Pfeifer, C. Monte, W. Pilz, A. Hoffmann, M. Spieles, K. Rurack, J. Hollandt, D. Taubert, B. Schonenberger and P. Nording, *Journal of Fluorescence*, 2005, 15, 315-336.
3. U. Resch-Genger, W. Bremser, D. Pfeifer, M. Spieles, A. Hoffmann, P. C. DeRose, J. C. Zwinkels, F. o. Gauthier, B. Ebert, R. D. Taubert, C. Monte, J. Voigt, J. Hollandt and R. Macdonald, *Analytical Chemistry*, 2012, 84, 3889-3898.
4. C. Würth, M. Grabolle, J. Pauli, M. Spieles and U. Resch-Genger, *Nature Protocols*, 2013, 8, 1535-1550.
5. J. N. Demas and G. A. Crosby, *Journal of Physical Chemistry*, 1971, 75, 991-1024.
6. P. C. DeRose and U. Resch-Genger, *Analytical Chemistry*, 2010, 82, 2129-2133.
7. J. H. Chapman, T. Förster, G. Kortüm, C. A. Parker, E. Lippert, W. H. Melhuish and G. Nebbia, *Applied Spectroscopy*, 1963, 17, 171-171.
8. S. E. Braslavsky, *Pure and Applied Chemistry*, 2007, 79, 293-465.
9. C. Würth, M. Grabolle, J. Pauli, M. Spieles and U. Resch-Genger, *Analytical Chemistry*, 2011, 83, 3431–3439.
10. C. Würth, J. Pauli, C. Lochmann, M. Spieles and U. Resch-Genger, *Analytical Chemistry*, 2012, 84, 1345-1352.
11. C. Wurth, C. Lochmann, M. Spieles, J. Pauli, K. Hoffmann, T. Schuttrigkeit, T. Franzl and U. Resch-Genger, *Applied Spectroscopy*, 2010, 64, 733-741.
12. T. S. Ahn, R. O. Al-Kaysi, A. M. Mueller, K. M. Wentz and C. J. Bardeen, *Review of Scientific Instruments*, 2007, 78, 086105.
13. L. Cademartiri, E. Montanari, G. Calestani, A. Migliori, A. Guagliardi and G. A. Ozin, *Journal of the American Chemical Society*, 2006, 128, 10337-10346.